Dynamics of a single cavitating and reacting bubble

Guillermo Hauke,* Daniel Fuster, and Cesar Dopazo
Departmento de Mecanica de Fluidos, Centro Politecnico Superior, C/Maria de Luna 3, 50.018 Zaragoza, Spain
(Received 7 April 2006; revised manuscript received 2 April 2007; published 19 June 2007)

Some of the studies on the dynamics of cavitating bubbles often consider simplified submodels assuming uniform fluid properties within the gas bubbles, ignoring chemical reactions, or suppressing fluid transport phenomena across the bubble interface. Another group of works, to which the present contribution belongs, includes the radial dependence of the fluid variables. Important fluid processes that occur inside the gas bubble, such as chemical reactions, and across the bubble interface, such as heat and mass transfer phenomena, are here considered also. As a consequence, this model should yield more realistic results. In particular, it is found that water evaporation and condensation are fundamental transport phenomena in estimating the dissociation reactions of water into OH. The thermal and mass boundary layers and the radial variation of the chemical concentrations also seem essential for accurate predictions.

DOI: 10.1103/PhysRevE.75.066310 PACS number(s): 47.55.dp, 47.70.−n, 47.11.−j

I. INTRODUCTION

Although cavitation is known as a fluid flow phenomenon that causes deterioration in the behavior and durability of hydraulic machines and installations [1], these days it is clearer that it can also be used to our benefit. The high temperature, pressure, and concentration of radicals make cavitating bubbles ideal microreactors which are able to enhance chemical conversion. This has already been used in medical and industrial applications, and in the environmental reduction of liquid waste and pollutants [2–4].

However, to this date, the mechanisms by which cavitation acts in all these processes is not completely understood. Initial studies of cavitating bubbles achieved great advances toward the understanding of cavitation, but were simplified models, either assuming, for example, uniform fluid properties within the gas bubbles or ignoring chemical reactions or transport phenomena across the bubble interface. For instance, Prosperetti and co-workers [5–7] conducted extensive studies of the dynamics of cavitating bubbles, ignoring chemical reactions and interface transport phenomena. Kamath *et al.* [8] tried to estimate the production of radicals from bubble temperature and pressure, with no coupling of the chemical reaction with the bubble dynamics. The model by Sochard *et al.* [9] included the diffusion of gases within the bubble and evaporation and condensation of water across the interface, while reactions were considered to be in thermodynamic equilibrium. Akhatov *et al.* [10] incorporated multiple transport phenomena across the bubble interface and used elaborate constitutive relations, neglecting chemical reactions. Gong [11] solved a model of a chemically reacting bubble with a uniform property model and without interface transfer phenomena.

More recently, extensive studies have been conducted by several authors [12–15] providing some insight into the processes taking place inside the bubble. The present formulation is similar to recent models such as that of Storey and Szeri [16] and those in Refs. [13–15,17], with slight improvements. Yasui *et al.* [17] developed a model to estimate OH; some restrictive approximations, such as using an approximate formula for the interface temperature calculation or assuming the bubble temperature and pressure as constant except in a thin layer, were used by these authors. An and Ying [15] proposed another complete single-bubble model; the liquid energy equation was solved neglecting the viscous dissipation and reaction processes, limiting the applicability of the model. Xu *et al.* [14] presented a complete model in which the radial variations of properties inside the bubble were considered. *Ad hoc* equations were used to calculate most of the gas and liquid properties; however, reactions were not taken into account, and the heat transfer across the interface was only approximately calculated. Lin *et al.* [13] have checked the validity of different hypotheses, like the radial pressure uniformity inside the bubble or the validity of the Rayleigh-Plesset equation; the range of conditions under which the homobaricity hypothesis holds has been clarified; again, no reactions were included in this model, thus neglecting an important source of inner bubble pressure gradients.

Perhaps the most similar models to the present contribution are those of Storey and Szeri [18,19], who suggested that the main reason for the sonoluminiscence phenomenon might be the water vapor trapped inside the bubble during implosion; this has also been pointed out by Colussi and Hoffmann [20]. In their work, complete single-bubble models, including chemical reactions as well as radial variations of properties inside the bubble, were presented, using a different method to track the bubble interface in comparison with the current model. However, the chemical processes taking inside the bubble and their effect on the bubble dynamics were not thoroughly investigated.

In this work, a detailed study of the coupled dynamics of the cavitating bubble and the surrounding liquid is conducted, including the radial dependence of the fluid variables. Important fluid processes that take place inside the gas bubble, such as chemical reactions, and across the bubble interface, such as the heat and mass transfer between the inner gas and the outer liquid, are considered. Here, the full liquid energy equation is solved and, in order to capture the interface dynamics and the mass transfer across the bubble interface, an arbitrary Lagrangian-Eulerian formulation is

*Electronic address: ghauke@unizar.es

used. Temperature, pressure, and concentration profiles are obtained and discussed in detail, shedding light on the chemistry dynamics, OH formation, and water vapor concentration inside the bubble. The variable radial dependence cannot be ignored if we wish to understand the complex dynamics of reacting cavitating bubbles.

II. THE MATHEMATICAL MODEL

Throughout this study, the gas bubble is assumed immersed in a liquid, isolated, and far away from other bubbles or walls, so the flow inside and outside the bubble is spherically symmetric. Therefore, the appropriate coordinate system is that of spherical coordinates, r, θ, ϕ. Due to the spherical symmetry, the partial derivatives of the variables with respect to θ and ϕ are zero, and the only velocity is radial, v_r, so $v_\theta = v_\phi = 0$.

A. Conservation equations

The time-dependent dynamics of a reacting fluid flow, applicable to both the gas bubble and to the surrounding liquid, is governed by the following set of partial differential equations:

$$\frac{D\rho}{Dt} + \frac{\rho}{r^2}\frac{\partial(v_r r^2)}{\partial r} = 0, \tag{1}$$

$$\rho\frac{DY_\alpha}{Dt} = -\frac{1}{r^2}\frac{\partial}{\partial r}(r^2 j_\alpha^{\mathrm{diff}}) + \dot{\omega}_\alpha, \tag{2}$$

$$\rho\frac{Dv_r}{Dt} = -\frac{\partial p}{\partial r} + \frac{1}{r^2}\frac{\partial}{\partial r}(r^2\tau_{rr}) - \frac{\tau_{\theta\theta} + \tau_{\phi\phi}}{r}, \tag{3}$$

$$\rho\frac{De}{Dt} = -p(\boldsymbol{\nabla}\cdot\boldsymbol{v}) - \frac{1}{r^2}\frac{\partial(r^2 q_r)}{\partial r} + \phi_v, \tag{4}$$

where t is the time coordinate, ρ is the fluid density, v_r is the fluid radial velocity, Y_α is the mass fraction of species α, j_α^{diff} is the diffusive mass flux of species α, $\dot{\omega}_\alpha$ is the reaction rate of the α component, p is the pressure, τ_{rr}, $\tau_{\theta\theta}$, and $\tau_{\phi\phi}$ are diagonal components of the viscous stress tensor, e is the specific internal energy, q_r is the radial heat flux, and ϕ_v is the viscous dissipation function. Moreover, the temperature will be denoted by T.

In (4) the radiation heat has been neglected. Due to the pressure of water vapor molecules and the high temperatures reached, this assumption might have to be reconsidered.

The position of the bubble interface is accurately tracked through an adaptive moving mesh with velocity v_r^m, and thus the equations are written in the arbitrary Lagrangian-Eulerian (ALE) framework [21,22], and the substantial (or material) derivative is expressed as

$$\frac{D\cdot}{Dt} = \frac{\partial\cdot}{\partial t} + (v_r - v_r^{\mathrm{m}})\frac{\partial\cdot}{\partial r} \tag{5}$$

Note that the above partial time derivative is not at constant spatial coordinate but at constant mesh node.

The radial diffusive heat and mass fluxes will follow the Fourier and Fick laws, respectively,

$$q_r = -\kappa\frac{\partial T}{\partial r} + \sum_{\alpha=1}^{N} j_\alpha^{\mathrm{diff}} h_\alpha, \tag{6}$$

$$j_\alpha^{\mathrm{diff}} = -\rho D_\alpha\frac{\partial Y_\alpha}{\partial r}, \tag{7}$$

where κ is the thermal conductivity coefficient and D_α the mass diffusion coefficient of species α.

1. Bubble equations

For the gas inside the bubble, the continuity equation (1), together with the species equations (2), are solved. After substitution of the constitutive relations, the momentum equation (3) can be expressed as

$$\rho_g\frac{\partial v_g}{\partial t} + \rho_g(v_g - v^{\mathrm{m}})\frac{\partial v_g}{\partial r} = -\frac{\partial p_g}{\partial r} + \frac{4}{3r^2}\frac{\partial}{\partial r}\left(r^2\mu_g\frac{\partial v_g}{\partial r}\right) - \frac{8}{3}\frac{\mu_g v_g}{r^2} - \frac{4}{3}\frac{v_g}{r}\frac{\partial\mu_g}{\partial r}. \tag{8}$$

In order to relate the thermodynamic properties inside the bubble, the perfect gas state equation is assumed:

$$p_g = \rho_g R_0 \sum_{\alpha=1}^{N}\frac{Y_\alpha}{W_\alpha}T_g, \tag{9}$$

where R_0 is the perfect gas universal constant, W_α is the molecular mass of species α, and the gas pressure p_g is the total pressure in the bubble, the sum of all partial pressures (including the water vapor).

For a mixture of calorifically perfect gases the specific mixture enthalphy h can be obtained as

$$h(T) = \sum_{\alpha=1}^{N} Y_\alpha h_\alpha = \sum_{\alpha=1}^{N} Y_\alpha\left(h_{f\alpha}(T_{\mathrm{ref}}) + \int_{T_{\mathrm{ref}}}^{T} c_{p\alpha}(T')dT'\right). \tag{10}$$

$h_{f\alpha}$ is the formation enthalpy of species α at the reference temperature T_{ref} and $c_{p\alpha}$ is the specific heat capacity at constant pressure.

Using all the above constitutive and state equations, the energy equation (4) can be transformed into an equation for the temperature, which for the gas phase and spherical symmetry is

$$\rho_g\bar{c}_p\frac{DT_g}{Dt} = \frac{Dp_g}{Dt} + \frac{1}{r^2}\frac{\partial}{\partial r}\left(r^2\kappa_g\frac{\partial T_g}{\partial r}\right) - \sum_{\alpha=1}^{N}(h_\alpha\dot{\omega}_\alpha) - \sum_{\alpha=1}^{N} c_{p\alpha}\frac{\partial T}{\partial r}j_\alpha^{\mathrm{diff}} + \frac{4}{3}\mu\left(\frac{\partial v_g}{\partial r} - \frac{v_g}{r}\right)^2 \tag{11}$$

where $\bar{c}_p$ is the average mixture specific heat.

The substantial derivative of the pressure Dp_g/Dt is related to the temperature by means of the perfect gas equation (9).

Chemical kinetics

In a general symbolic form, the set of reactions (or reaction mechanism) that occurs inside the bubble can be represented as follows:

$$\sum_{\alpha=1}^{N} \nu'_{k\alpha}\chi_\alpha \rightleftharpoons \sum_{\alpha=1}^{N} \nu''_{k\alpha}\chi_\alpha \tag{12}$$

where $\nu'_{k\alpha}$ and $\nu''_{k\alpha}$ are the reactant and product stoichiometric coefficients, χ_α represents the chemical symbol of each compound, N is the total number of compounds considered in the mechanism, and k is the reaction number in the chemical scheme with K reactions.

Given a reaction and a compound, the coefficient $\nu_{k\alpha}$ is defined as

$$\nu_{k\alpha} = \nu''_{k\alpha} - \nu'_{k\alpha}. \tag{13}$$

If all steps (12) are elemental reactions, the chemical conversion rate of the reaction k can be obtained as

$$(-r_k) = k_{fk}\prod_{\alpha=1}^{N} C_\alpha^{\nu'_{k\alpha}} - k_{rk}\prod_{\alpha=1}^{N} C_\alpha^{\nu''_{k\alpha}} \tag{14}$$

where $(-r_k)$ is the reaction rate of the step k, C_α is the molar concentration, and k_{fk} and k_{rk} are the forward and reverse reaction kinetic constants. These kinetic constants are calculated from the Arrhenius expression,

$$k_{fk}(T) = A_k T^{\beta_k} \exp\left(-\frac{E_k}{RT}\right) \tag{15}$$

where A_k is the preexponential factor, β_k is constant, and E_k is the activation energy.

The reaction rates of each elemental step are added to get the global reaction rate of the compound α:

$$\dot{\omega}_\alpha = \sum_{k=1}^{K} (W_\alpha \nu_{k\alpha}(-r_k)). \tag{16}$$

B. Liquid equations

In a real liquid, variations of pressure and temperature may cause slight changes in density, where even a few percent density variation may have a profound effect on the flow features.

In order to diminish the computational cost of the model, the liquid continuity and momentum equations are combined and replaced by the Rayleigh-Plesset equation [1,23], introducing the liquid compressibility effects due to Keller and Miksis [24]. Thus, at $r=R(t)$,

$$\left(1-\frac{\dot{R}}{c}\right)R\ddot{R} + \frac{3}{2}\left(1-\frac{\dot{R}}{3c}\right)\dot{R}^2 = \frac{1}{\rho_l}\left(1-\frac{\dot{R}}{c}\right)[p_l - p_\infty(t)] + \frac{R}{\rho_l c}\frac{\partial p_l}{\partial t}, \tag{17}$$

where $R(t)$ is the bubble radius, c is the pressure wave velocity in the liquid (taken as a constant), $\dot{R}$ and $\ddot{R}$ are the velocity and the acceleration of the interface, respectively, p_l is the liquid pressure evaluated at the interface $r=R(t)$, p_∞ is the liquid pressure far away from the bubble, and ρ_l is the liquid density.

When the mass transfer is included, the Rayleigh-Plesset equation must be modified to take into account this phenomena, giving rise to the following ordinary differential equation at $r=R(t)$:

$$\left(1-\frac{\dot{R}}{c}-\frac{\dot{m}''}{\rho_l c}\right)R\left(\ddot{R}+\frac{\ddot{m}''}{\rho_l}\right) + \frac{3}{2}\left(1-\frac{\dot{R}}{3c}-\frac{2\dot{m}''}{3\rho_l c}\right)\dot{R}^2 + \frac{\dot{m}''}{\rho_l}\left(\dot{R}-\frac{\dot{m}''}{2\rho_l}-\frac{\dot{m}''\dot{R}}{2\rho_l c}\right) = \frac{1}{\rho_l}\left(1-\frac{\dot{R}}{c}\right)[p_l - p_\infty(t)] + \frac{R}{\rho_l c}\frac{\partial p_l}{\partial t}, \tag{18}$$

where $\dot{m}''$ is the evaporation-condensation mass flux (see, for instance, [25]). The value of $p_\infty(t)$ is a given function,

$$p_\infty(t) = p_0 + p_a \cos(2\pi f t), \tag{19}$$

where f is the frequency of the externally imposed pressure wave and p_a is its amplitude.

In order to relate the pressures at both sides of the interface, the momentum balance yields [25,26] at $r=R(t)$

$$p_g = p_l + \frac{4\mu_l \dot{R}}{R} + \frac{2\sigma}{R} + (\dot{m}'')^2\left(\frac{1}{\rho_l}-\frac{1}{\rho_g}\right), \tag{20}$$

where the gas viscous stresses have been neglected.

The liquid energy equation, neglecting here any variation of the density with temperature, is

$$\rho_l c_p \frac{DT_l}{Dt} = \frac{1}{r^2}\frac{\partial}{\partial r}\left(r^2 \kappa_l \frac{\partial T_l}{\partial r}\right) + \frac{4}{3}\mu_l\left(\frac{\partial v_l}{\partial r}-\frac{v_l}{r}\right)^2 \tag{21}$$

C. Mass transfer equations

The mass balance across the bubble interface is given by

$$\dot{m}'' = \rho_g(v_g(R,t)-\dot{R}) = \rho_l(v_l(R,t)-\dot{R}). \tag{22}$$

In this study, it will be assumed that the total mass transfer across the interface is solely given by the total water mass flux [10,12,17],

$$\dot{m}'' = -j^{\text{tot}}_{\text{H}_2\text{O}} \tag{23}$$

where $j_{\text{H}_2\text{O}}$ denotes the water mass flux by evaporation and condensation at the interface.

Cavitation is a sufficiently fast process that the equilibrium hypothesis may break down at the interface. For this reason, instead of using the equilibrium concentration at $r=R(t)$, the mass flux across the interface is calculated by means of the Hertz-Knudsen-Langmuir expression [27,28], derived from the kinetic theory of gases,

$$j_{H_2O}^{tot} = \frac{\beta(p_{sat} - p_{H_2O})}{\sqrt{2\pi \frac{R_0}{\bar{W}} T_{int}}}. \quad (24)$$

The saturation pressure p_{sat} at the interface conditions is computed using Antoine's correlation and the water coefficients included in [29]. This correlation replaces the classical Clausius-Clapeyron equation. Furthermore, p_{H_2O} is the partial vapor pressure of water, and T_{int} the liquid temperature, both at the interface. $\beta \in [0,1]$ is the accommodation coefficient, and represents the efficiency of the total number of molecules colliding at the interface. It is calculated as a function of T_{int}, interpolating the results of the molecular dynamics simulations by Matsumoto with the Gregory-Newton formula (as suggested in [25] to carry out bubble cavitation simulations). The correlation used is

$$\beta = \begin{cases} 0.35 & \text{if } T_{int} < 350 \text{ K}, \\ 0.35 - 0.05k^{(1)} - 0.05k^{(2)} + 0.025k^{(3)} & \text{if } 350 \leqslant T_{int} \leqslant 500 \text{ K}, \\ \dfrac{0.05}{T_c - 500}(T_c - 500) & \text{if } 500 \text{ K} \leqslant T_{int} \leqslant T_c, \\ 0 & \text{if } T \geqslant T_c, \end{cases} \quad (25)$$

with

$$k^{(m)} = k(k-1)\cdots[k-(m-1)] \quad (26)$$

and

$$k = \frac{T_{int}}{50} - 7, \quad (27)$$

where T_c is the critical temperature.

During the collapse it is possible to reach supercritical conditions. As has been discussed by other authors [10], it can be considered that there is no water mass flux when the temperature at the interface is higher than the critical temperature. The short period during which those conditions are attained will have a negligible effect in the calculation of the bubble dynamics.

D. Additional boundary conditions

At the bubble center, spherical symmetry implies no radial gradient, i.e.,

$$\frac{\partial Y_\alpha}{\partial r} = \frac{\partial \rho_g}{\partial r} = \frac{\partial T_g}{\partial r} = 0, \quad r = 0, \quad \forall\ t. \quad (28)$$

Moreover, the velocity at the center of the bubble is zero:

$$v_g = 0, \quad r = 0, \quad \forall\ t \quad (29)$$

and

$$\frac{\partial v_g}{\partial r} = 0, \quad r = 0, \quad \forall\ t. \quad (30)$$

From the continuity condition at the interface (22), the evaporation flux (24), and the interface velocity $\dot{R}$, calculated from (17), the gas velocity at the interface $v_g(R,t)$ can be obtained as

$$v_g(R,t) = \dot{R} - \frac{j_{H_2O}}{\rho_g}. \quad (31)$$

The total flux of species α across the interface, j_α^{tot}, is calculated as the sum of the advective flux j_α^{adv} and the diffusive flux j_α^{diff}. Therefore, the balance at $r=R(t)$ implies

$$\dot{m}'' Y_\alpha^l - \rho_l D_\alpha^l \frac{\partial Y_\alpha^l}{\partial r} = \dot{m}'' Y_\alpha^g - \rho_g D_\alpha^g \frac{\partial Y_\alpha^g}{\partial r}, \quad (32)$$

where the superscripts g and l indicate the gas and liquid phases, respectively.

As in the current model only water is considered in the liquid (i.e., $Y_{H_2O}^l = 1$, $Y_\alpha^l = 0\ \forall\ \alpha \neq H_2O$), the equation can be written as

$$\dot{m}'' Y_\alpha^l = \dot{m}'' Y_\alpha^g - \rho_g D_\alpha^g \frac{\partial Y_\alpha^g}{\partial r}, \quad (33)$$

where $\dot{m}''$ can be related to the velocities at the interface by means of the mass balance (22), and D_α is the diffusion coefficient. Substituting in (33) and reorganizing terms, at $r=R(t)$,

$$j_\alpha^{tot} = \rho_g (v_g - \dot{R}) Y_\alpha^g - \rho_g D_\alpha \frac{\partial Y_\alpha^g}{\partial r}, \quad (34)$$

where j_α^{tot} is the variable that is imposed to solve the individual component equations (2), and the water mass flux is set by means of (24). Therefore, this model assumes that the

TABLE I. Initial species concentrations inside the bubble.

Species	Molar fraction	Mass fraction
Ar	0.954	0.979
H_2O	0.046	0.021

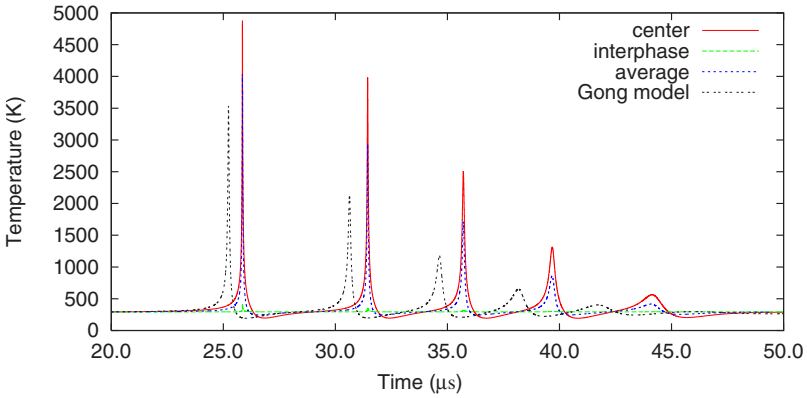

FIG. 1. (Color online) Zoom to the first series of peaks.

flux of other species across the bubble interface is negligible.

The heat balance at the interface establishes the relation among the heat fluxes on the liquid and gas sides:

$$-\kappa_l \frac{\partial T_l}{\partial r} + (v_l - \dot{R})\rho_l h_l - \rho_l \sum_{\alpha=1}^{N} h_\alpha^l D_\alpha^l \frac{\partial Y_\alpha^l}{\partial r} = -\kappa_g \frac{\partial T_g}{\partial r} + (v_g - \dot{R})\rho_g h_g - \rho_g \sum_{\alpha=1}^{N} h_\alpha^g D_\alpha^g \frac{\partial Y_\alpha^g}{\partial r}, \quad (35)$$

which can be approximated by using the latent heat of evaporation,

$$\kappa_l \frac{\partial T_l}{\partial r} = \kappa_g \frac{\partial T_g}{\partial r} + \Delta H_{\text{vap}} j_{H_2O}, \quad r = R(t). \quad (36)$$

The variation of the enthalpy of vaporization with the temperature, ΔH_{vap}, is calculated from the Watson equation [30],

$$\Delta H_{\text{vap}} = \Delta H_{\text{vap}}^0 \left(\frac{T_c - T}{T_c - T_{\text{bp}}} \right)^{0.38}, \quad (37)$$

where T_{bp} is the normal boiling point.

The numerical procedure assumes a continuous temperature profile across the interface. Although this hypothesis can be questioned when the evaporation fluxes are very high during the implosion, it is considered as a first approximation that its effect on the results is negligible.

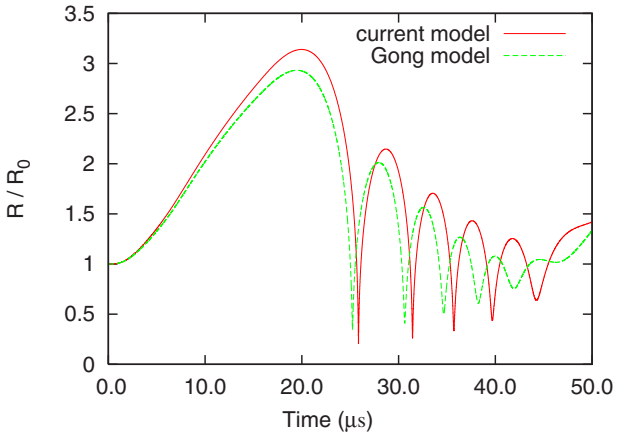

FIG. 2. (Color online) Bubble radius evolution.

In the literature, there are many available models to predict the temperature jump at the interface, which, however, for a given evaporation flux, predict very scattered values of the temperature jump. Moreover all of these correlations are a function of the accommodation coefficient, which increases the uncertainty of the results given by such correlations. The numerical procedure assumes, thus, a continuous temperature profile across the interface,

$$T_g = T_l, \quad r = R(t). \quad (38)$$

Finally, one more condition is required to solve the energy equation. This is selected as the liquid temperature far away from the bubble, which can be considered constant and equal to the bulk liquid temperature. Thus,

$$T_l = T_\infty \quad (r \to \infty). \quad (39)$$

The fluid velocity at the interface, which is used as a boundary condition to solve the momentum equation in the gas phase, is related to the interface velocity and the evaporation flux. Indeed, Eq. (31) determines the velocity of the gas once $\dot{R}$ and j_{H_2O} are calculated.

E. Initial conditions

In order to specify the initial conditions it is assumed that the bubble is initially in equilibrium with the surrounding

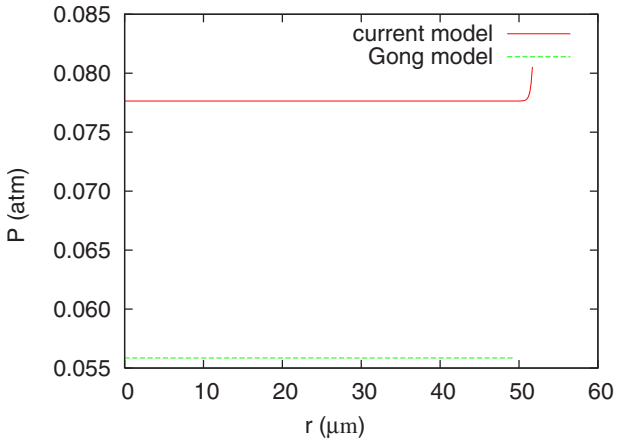

FIG. 3. (Color online) Radial pressure profile inside the bubble during the expansion ($t = 1.47 \times 10^{-5}$ s).

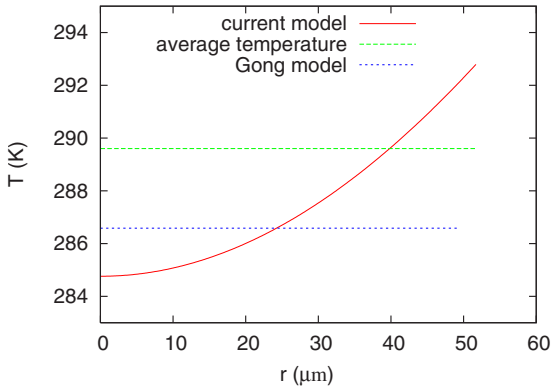

FIG. 4. (Color online) Radial temperature profile inside the bubble during the expansion ($t=1.47\times10^{-5}$ s).

liquid and there is no gradient associated with any of the problem variables. This implies that the initial interface velocity is zero ($\dot{R}=0$), the bubble temperature is constant and equal to the liquid temperature, and the initial fluid velocities are zero. The liquid pressure far away from the bubble, p_∞, is given, so the initial internal bubble pressure can be calculated by means of the momentum balance at the interface from Eq. (20). The initial gas density can be calculated from the bubble pressure and temperature. Finally, the initial concentrations are specified data, with the exception of the water concentration, which is calculated from the equilibrium conditions.

F. Solution method

The above nonlinear system of coupled partial differential equations is solved with an ALE [21] finite element method combined with a 5/6-order Fehlberg Runge-Kutta method (including the Cash and Karp modification) with adaptive time step and error control [31].

The CHEMKIN package has been used to calculate the different properties as a function of the composition, concentration, and thermodynamic properties. This package contains a database with the thermodynamic information for different substances, and it allows one to introduce new compounds if the required information is known.

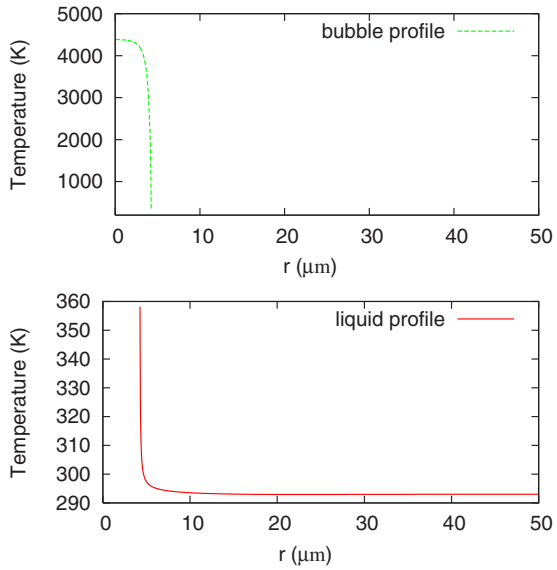

FIG. 5. (Color online) Temperature profile in the gas and liquid during the implosion.

In general, the diffusion coefficients depend on pressure, temperature, and chemical concentrations, $\mu(p,T,Y_\alpha)$, $\kappa(p,T,Y_\alpha)$, and $D_\alpha(p,T,Y_\alpha)$. However, the numerical simulations show that the gas viscosity variation has an insignificant influence on the final results, and therefore, in order to reduce the CPU time, the viscosity was taken as a constant. The same reasoning can be applied to the liquid, where the conditions are not as extreme as inside the bubble.

Likewise for the thermal conductivity, the hypothesis of constant thermal conductivity can be used during the whole simulation except at the bubble implosion. But at that time, the critical conditions are generally exceeded inside the bubble, creating a high uncertainty in its evaluation. Further-

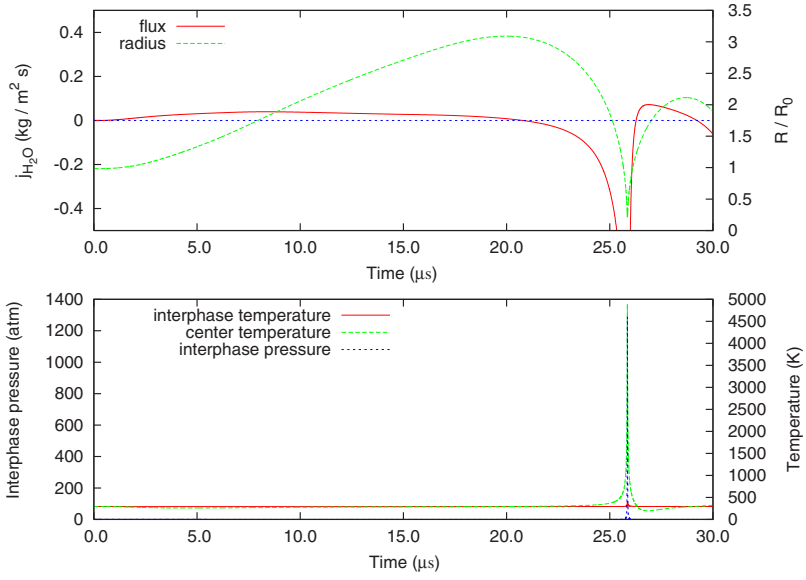

FIG. 6. (Color online) Temporal evolution of the bubble radius, evaporation flux, center and interface bubble temperature, and interface pressure until the first implosion.

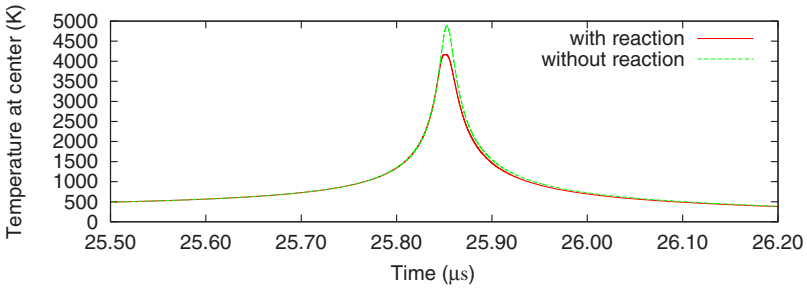

FIG. 7. (Color online) Argon bubble with dissociation. Influence of the dissociation reactions on the temperature evolution at the main peak.

more, studies by other authors show that the temperature dependence of the thermal conductivity has a negligible influence on the solution.

Finally, the diffusion coefficients D_α have been computed from the CHEMKIN physical properties database, taking into account the temperature and concentration dependence.

III. DYNAMICS OF ULTRASOUND-INDUCED CAVITATING BUBBLES

In order to illustrate the potential of the present model, three examples are considered. The first two consist of an argon bubble with and without dissociation reactions, respectively. In these first two examples, the water vapor content inside the bubble originates from mass transfer across the bubble interface. In the third example, combustion reactions of H_2 and O_2 are studied inside a bubble with Ar and water content.

A. Inert argon bubble

The first example consists of the simulation of an inert Ar plus H_2O bubble, weakly excited by a pressure amplitude of $p_a=1.2$atm at a frequency of $f=22.3$ kHz. The bubble has an initial radius of 19.3 μm and the initial concentrations are included in Table I.

Figure 1 compares the bubble temperature at its center, at its interface, and the average value, obtained by the present model and that of Gong [11], where constant properties inside the gas bubble are assumed, no mass transfer at $r=R(t)$ is accounted for, and the heat transfer across the interface is calculated approximately from transport coefficients. Significant differences between the two models are apparent in the peak temperatures as well as in the times of the occurrence of the spikes.

The results in [11] allow the forcing pressure in the liquid to go below its vapor pressure, which may be unphysical. This artificially boosts the maximum temperatures and pressures inside the bubble. On the other hand, in this work the driving pressures are limited to be always above the fluid vapor pressure.

A zoom to the first series of rebounds is depicted in Fig. 1, where history effects are diminished and the influence of modeling is stressed. Since the present model includes the radial variation of the fluid variables and interface transport phenomena, it is expected to yield more realistic temperatures than that of Gong. In particular, the present model predicts larger temperatures at the center of the bubble, but lower temperatures at the interface, due to the cooling effect caused by the liquid. Thus, the temperature at the interface (around 500 K) is lowered to values reported by other authors [2].

The reason for the larger temperatures at $r=0$ calculated by the current model (shown in Fig. 1) can be seen in Figs. 2–4. During the initial preimplosion expansion, the Gong model uses a spatially uniform pressure inside the bubble, which at the interface and during the expansion is lower than the actual pressure, reducing the maximum bubble radius.

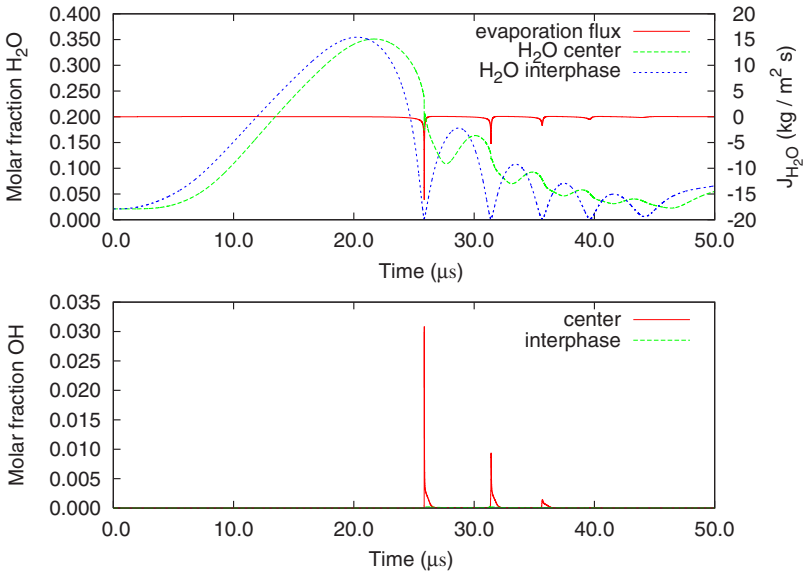

FIG. 8. (Color online) Argon bubble with dissociation. Zoom of the concentrations during the first peak series, including the evaporation rate.

TABLE II. Initial concentrations for a reacting bubble.

Compound	Molar fraction	Mass fraction
Ar	0.365	0.479
H_2O	0.036	0.021
O_2	0.468	0.491
H_2	0.131	0.009

However, in the present model, the pressure does not decrease so fast for two reasons. On the one side, the liquid thermal boundary layer transfers heat to the interface, raising the gas pressure. On the other hand, the evaporation process tends also to increase the gas density and the gas pressure. The latter enhances the expansion process, which later makes the collapse more violent.

The pressure within the bubble displays a large degree of spatial uniformity during most of the evolution time. However, as the characteristic times for evaporation and for pressure wave propagation become of the same order, a slight increase of pressure appears at $r=R(t)$, as is depicted in Fig. 3 (for $t=1.47\times10^{-5}$ s). This behavior does not appear in the absence of mass transfer across the interface. Due to the evaporation process, there is a net flux inward to the bubble at $r=R(t)$ that locally increases the density and pressure there. A pressure of the order of 3% higher than at $r=0$ is predicted at the grid point coinciding with the interface; this has an effect on the bubble dynamics. Higher pressure at the interface produces larger expansions, as can be seen in Fig. 2. Therefore, the current model predicts a more intense expansion process and, consequently, larger radii. This feature of the present model is consistent with the finding of Lin *et al.* [13] on pressure spatial uniformity within the bubble.

The gas and liquid temperature fields are displayed in Fig. 5 when the temperature reaches the maximum peak during the second series of rebounds. Inside the gas, the temperature varies across the whole bubble radius. In the liquid, the thermal boundary layer thickness is of the order of magnitude of the bubble radius. Clearly, for an accurate heat transfer prediction, the time-dependent radial variation of temperature across the fluids cannot be neglected.

The prediction of the radial profiles allows us to establish the different stages of evaporation and condensation which occur at the interface (Fig. 6). Note that the evaporation and condensation rates might be critically dependent upon Eq. (24), used in this work. Consideration of the radiation heat transfer from the emitting molecules (mainly water vapor) within the bubble toward the interface might also significantly alter the present picture, which should only be considered as a first approximation to a complicated phenomenon.

During most of the expansion, evaporation is produced as a consequence of the low pressure at the interface. Then, bubble expansion is followed by compression, where the high pressures induce condensation conditions at $r=R(t)$. After the bubble collapses (point of minimum bubble radius), condensation is still predicted during the first moments of the expansion process. But as the interface pressure decreases below the equilibrium pressure, evaporation is predicted again, to repeat the cycle.

In this case, condensation conditions have been predicted during the whole compression stage; however, it has been found that this process is strongly influenced by the rate of change of temperature and pressure at $r=R(t)$. Increases of these two properties have opposite effects on the evaporation and condensation processes. High temperatures tends to evaporate liquid water whereas high gas pressures enhance water vapor condensation. For this reason, depending on which effect dominates, either evaporation or condensation is predicted at the interface. This feature has been observed in the results obtained by the current model. In particular, the value of $C_{p,l}$ has an impact on which of the two effects is more relevant. For instance, lower $C_{p,l}$ values imply higher interface temperatures during the compression stage, enabling evaporation during the implosion. However, at values of $C_{p,l}$ around the liquid water value, the temperatures at the interface are lower, and the high pressure at the interface produces condensation during the compression stage.

Although the value of $C_{p,l}$ has been used to artificially modify the relevance of temperature increments over pres-

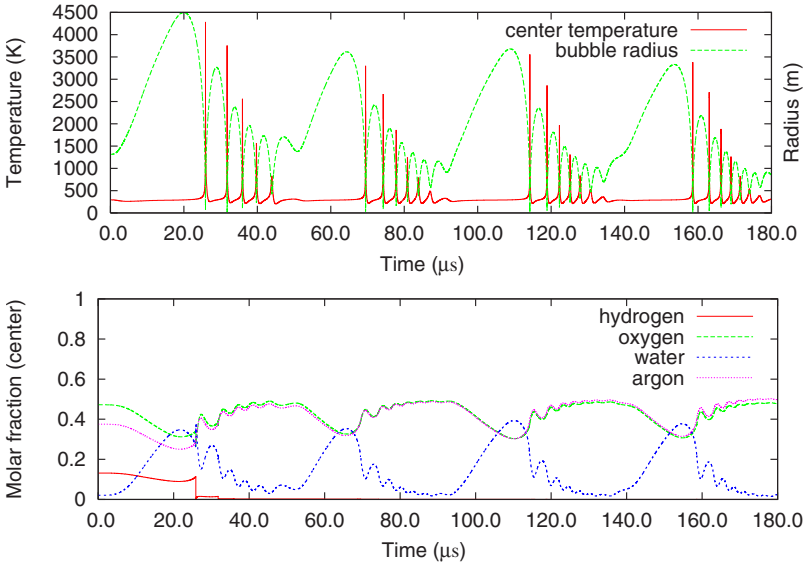

FIG. 9. (Color online) Reacting bubble. Temporal evolution of the temperature and molar concentrations at the bubble center

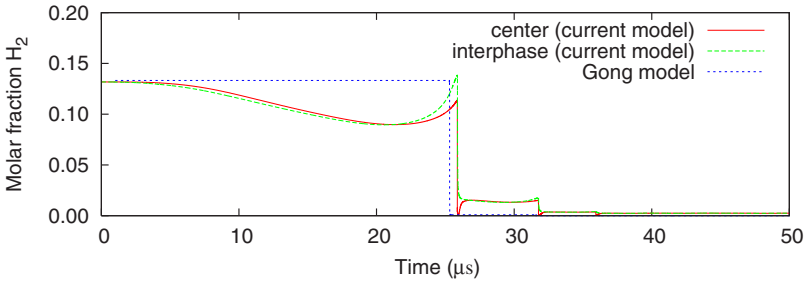

FIG. 10. (Color online) Reacting bubble. Temporal evolution of hydrogen molar concentration in the bubble.

sure increments, it is important to remark that any process which makes the interface temperature increase more quickly than the pressure can have a similar influence on the evaporation and condensation processes at $r=R(t)$. In this way, perhaps some processes such as radiation, which have been not taken into account, might have significant effect upon the evaporation and condensation.

One of the advantages of the present model is the capability of predicting dynamic water vapor interface transport and concentration profiles inside the bubble. Although the initial models neglected the water content inside the bubble, Moss *et al.* [32] showed that the water concentration inside the bubble is one of the most sensitive parameters to determine the emission from a sonoluminiscence bubble. The model by Storey and Szeri [16] was the first able to predict water concentrations, and it was found that the water vapor is trapped inside the bubble due to the short time of the collapse. According to them, the water vapor inside the bubble does not have enough time to diffuse toward the interface, where condensation conditions are predicted during the whole compression stage, which is in agreement with the present results.

In general, mass transfer decreases the fluid temperature at the interface. When mass transfer is taken into account solely in the energy equation, this is basically the only physical consequence, which manifests very strongly. However, when mass transfer is considered in all the equations, the physical effects become more intricate. For instance, during the bubble implosion, there is condensation, which modifies the calculated bubble dynamic behavior.

B. Argon bubble with dissociation reactions

This case is identical to that of the previous section, but allowing for dissociation reactions. The H_2 and O_2 chemical kinetics is also used for the reacting H_2 and O_2 bubble (Sec. III C), since this mechanism includes dissociation reactions. At around 3000 K water molecules begin to dissociate into OH and H [20,33]. This dissociation is an endothermic process that reduces the temperature at the implosion (see Fig. 7). During the expansion, the radicals recombine through an exothermic process. However, this process is shown not to greatly influence the calculated temperatures, at least for the considered cases. As the temperature increases, this phenomenon is more relevant to the dynamics of the bubble.

Despite having no great effect in the temperature profiles, the reaction mechanism allows us to predict OH concentrations inside the bubble. The OH concentration gives an estimate of the dissociation and the effectiveness of the bubble as a microreactor.

However, as the concentration of OH depends on the water concentration, models with no evaporative mass transfer, like [11], cannot predict correctly the evolution of this radical nor the dissociation process. For instance, for an argon bubble, models with no evaporative mass transfer through the interface would predict a zero concentration of water. For bubbles with other initial chemical concentrations, the OH evolution will depend on the chemical kinetics and on the initial water concentration. Thus, in the current model, the radial variation of the water composition inside the bubble and the mass transfer across the interface allow improvement in the computation of OH profiles.

As the concentration of OH depends on water concentration, these models are not able to predict the dissociation correctly. However, in the current model, the radial variation of the water composition inside the bubble and the mass transfer across the interface allow some improvement in the computation of OH profiles. Note that the increment of water concentration during the evaporation stage (as commented in the previous subsection) enhances OH formation.

Figure 8 shows that the OH concentration is much more important at the center than at the interface, where, due to the low temperature, no dissociation reactions take place. Thus, the presence of OH at the interface can be accounted for only by diffusion transport from the bubble center.

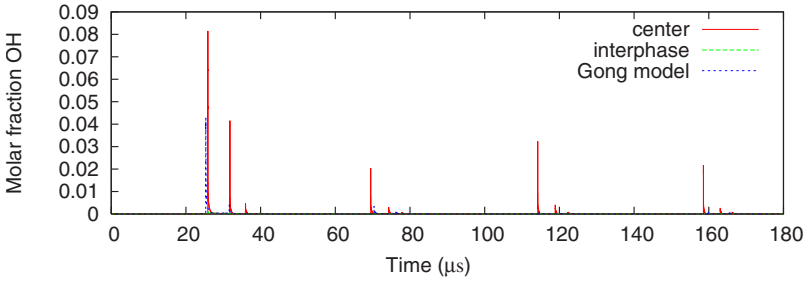

FIG. 11. (Color online) Reacting bubble. Comparison among the OH molar concentrations in each peak series.

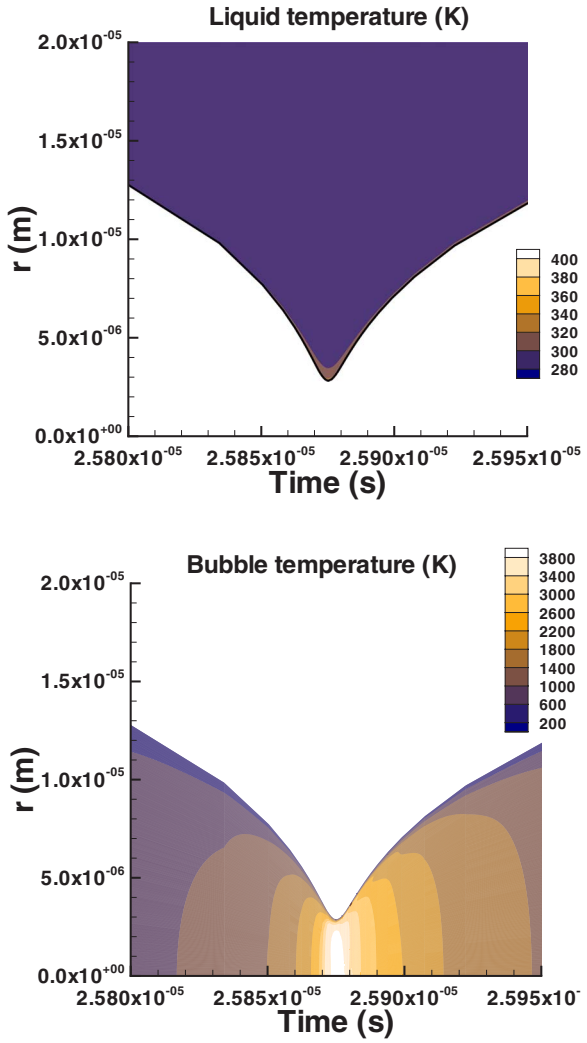

FIG. 12. (Color online) Main peak of the first series of rebounds. Liquid and gas temperature profiles during the bubble collapse.

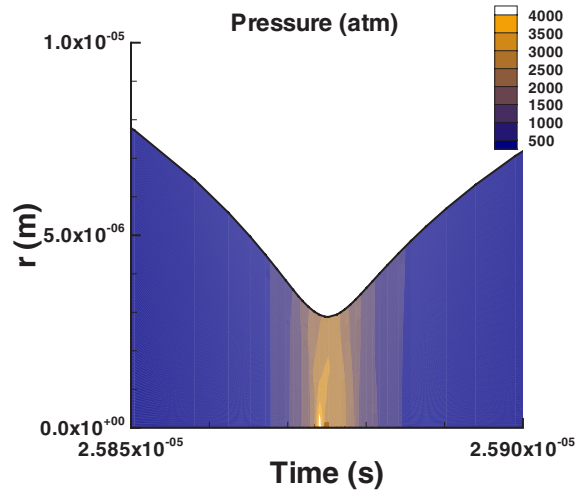

FIG. 13. (Color online) Main peak of the first series of rebounds. Pressure profile during the bubble collapse.

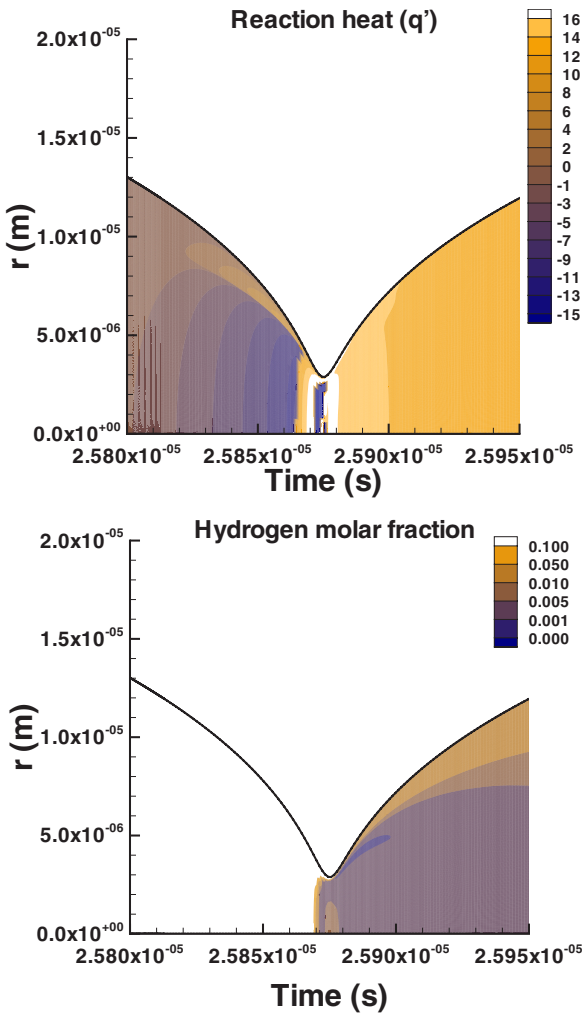

FIG. 14. (Color online) Main peak of the first series of rebounds. Radial distribution of reaction heat and hydrogen molar fraction.

C. Reacting Ar, H_2, O_2, H_2O bubble

The third example consists of the simulation of an Ar, H_2, O_2, and H_2O reacting bubble, with a sonochemical excitation of p_a=1.2 atm and f=22.3 kHz.

The aim of this section is at showing different reaction processes that can occur in a bubble. It is important to remark that no reliable chemical data are available for temperatures higher than 3000 K. As a first approximation, and due to the short duration of such conditions, it has been decided to extrapolate the calculated chemical reaction rates, being aware of the uncertainty and some loss of accuracy. However, this should be considered as an attempt at studying the chemical phenomena that take place inside the bubble.

The initial radius is 19.3 μm and the starting concentrations are included in Table II.

CHEMKIN is used with the mechanism of Allen *et al.* [34] extracted from Akbar *et al.* [35]. This mechanism uses nine compounds (H, H_2, O, OH, O_2, OH_2, H_2O, H_2O_2, and Ar) and 26 elemental equations (including third-body reactions and SRI pressure-dependent reactions).

As will be seen, the Gong model predicts the complete consumption of the H_2 at the first implosion, whereas in the

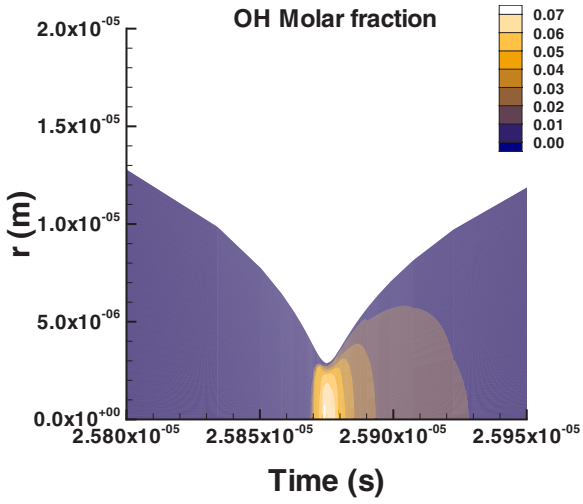

FIG. 15. (Color online) Main peak of the first series of rebounds. OH molar fraction profile during the bubble collapse.

present model only a fraction reacts. Therefore, the faster conversion predicted by Gong increases the heat release during the first peak. For this reason, although the compression is not so violent in the Gong model, the higher heat generation increases the temperature at the center up to the same value predicted by the current model.

Figure 9 shows that the peak temperatures are attained at the minimum bubble radii, where, simultaneously, the reaction processes take place, consuming H_2 and O_2 and producing water.

As the temperature and pressure rise, the strong radial dependence of the reaction rates prevents all the hydrogen from being consumed during the first implosion. At the interface the reaction rates are much slower than at the center, producing a strong gradient in the hydrogen composition.

During the expansion, the hydrogen not consumed near the interface diffuses to the center very quickly because of the large concentration gradient. When the next implosion occurs, the hydrogen at the bubble center reacts very quickly again, while the reaction rate at the interface is much slower. Thus, the hydrogen is not consumed in one step, as in the Gong model, but takes two cycles to disappear.

After that, the bubble enters an approximately periodic state. Figure 10 shows in more detail the hydrogen temporal evolution at the center and at the interface, which is also compared to the results of Gong.

Figure 11 shows the OH production. Again, the uniform model predicts that the reaction should occur at the first peak, showing little dissociation thereafter. However, because of the mass transfer across the interface, the present model is able to supply and remove water and enhance the OH production.

A more detailed analysis will be presented below.

The next set of figures depicts space-time contour plots of the flow field. The following three cases can be found depending on the reactant concentration: (1) None of the reactants (H_2 and O_2) are consumed during the collapse. (2) The limiting reactant is consumed before the maximum compression is reached (which can be due to a high reaction rate or a low reactant concentration). (3) There are no reactants and only dissociation reactions occur. This is the case of the Ar bubble.

The following series of rebounds capture the above cases clearly. In Figs. 12–16 the hydrogen is consumed neither at the bubble center nor at the interface. There are different stages in the implosion-expansion process. At the beginning of the compression stage there is a dissociation of the water molecules at the center (which is an endothermic process) while at the interface such conditions are not achieved. The radicals diffuse toward the interface, where dissociation conditions are not met (due to the lower temperatures) and exothermic association processes take place (yellow reaction heat).

When the temperature and pressure are high enough to begin the hydrogen-oxygen combustion, the exothermic processes become more relevant. As a general rule, such conditions are reached before the maximum compression moment.

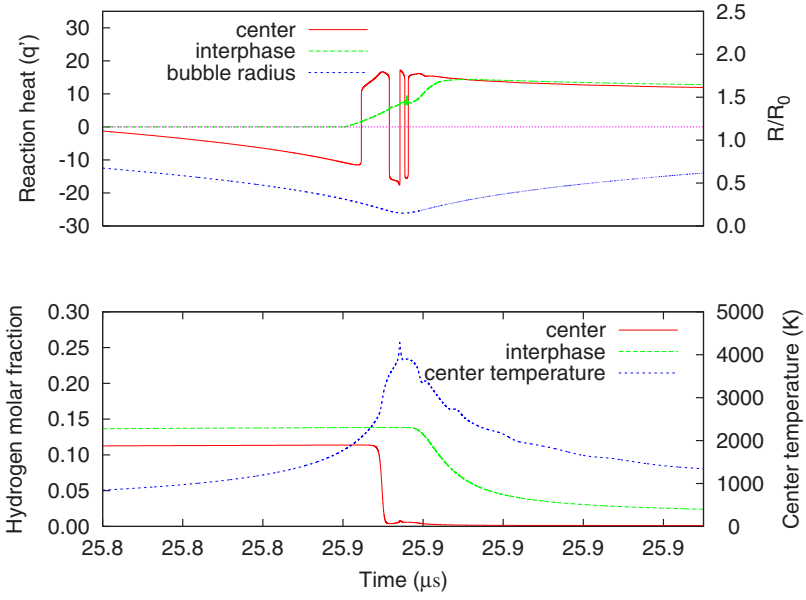

FIG. 16. (Color online) Evolution of the concentrations and reaction heat in the main peak of the first series.

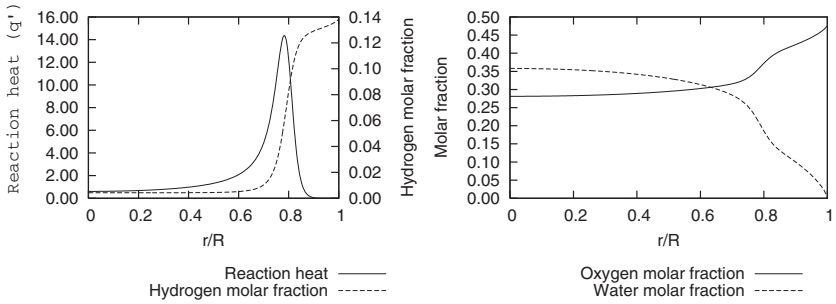

FIG. 17. Profiles during the combustion at the main peak of the first cycle. Radial profiles of reaction heat and molar concentrations ($t=2.5827\times10^{-5}$ s).

Then, a very quick consumption of hydrogen starts at the center and advances toward the interface, even during the expansion, until the temperature and pressure are lowered to values at which the reaction cannot take place.

Figures 17 and 18 show the radial dependence of the fluid variables and chemical concentrations at a particular moment during the expansion, when reaction is occurring.

As the reaction heat q can vary by several orders of magnitude and can be either positive (exothermic reaction) or negative (endothermic reaction), the modified expression

$$q' = \begin{cases} \mathrm{sgn}(q)\log_{10}|q|, & |q| > 1, \\ 0, & |q| \leqslant 1, \end{cases} \tag{40}$$

has been used to portray the heat release in a logarithmic scale with its sign.

From the heat release profile, two reaction zones can be observed inside the bubble, separated by the flame front (characterized by a large reaction heat).

As a consequence of the more extreme conditions at the bubble center, the hydrogen (the limiting reactant in this particular case) reacts at the bubble center sooner than at the interface, causing the flame front to propagate toward the interface. At the bubble center, because of the combustion, the hydrogen has been practically exhausted, the concentration of O_2 has decreased, and that of water, a reaction product, has increased. The positive heat release is a consequence of the slight temperature decrease caused by the expansion process, which modifies the equilibrium, causing the formed radicals to recombine in an exothermic process.

The combustion process raises the temperature (Fig. 18), producing a high radial temperature gradient at the flame front. The linear velocity profile around the center is in agreement with the uniform density profile there.

Moreover, at the interface a thin boundary layer is observed due to evaporative mass transfer. During these initial expansion moments, an evaporation flux is predicted, lowering the concentrations of all components except that of water. This mass flux is responsible for the sharp increase of density and pressure at $r=R(t)$.

The effect of the reaction in the bubble dynamics is higher when the reaction rate is faster (normally due to higher temperature). The higher the temperature, the more important the reaction processes inside the bubble become.

In the third series of rebounds, (Figs. 19 and 20), when all reactants are completely exhausted, the bubble contains mainly water and argon. This situation is analogous to the argon bubble when dissociation processes are taken into account. Water molecules dissociate during the compression and afterward a recombination of the radicals occurs when the bubble grows. As the conditions at the center are more extreme than at the interface, there is a strong gradient of radicals, which diffuse to the interface. As the conditions at $r=R(t)$ are not as severe as at $r=0$, the radicals react to produce elemental water molecules, and, thus, a positive reaction heat flux appears at the interface (within a very thin boundary layer).

Very important radial variations of the properties are evident. If reaction processes are included, exothermic and endothermic zones can simultaneously coexist inside the bubble, inducing important gradients of concentrations.

IV. CONCLUSIONS

This paper numerically simulates the dynamics of ultrasound cavitating bubbles, including the radial variation of the fluid variables, both in the gas and in the liquid. Inside the

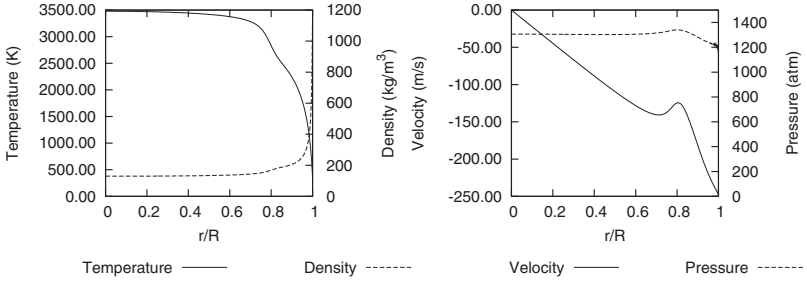

FIG. 18. Profiles during the combustion at the main peak of the first cycle. Radial profiles of the fluid variables ($t=2.5827\times10^{-5}$ s).

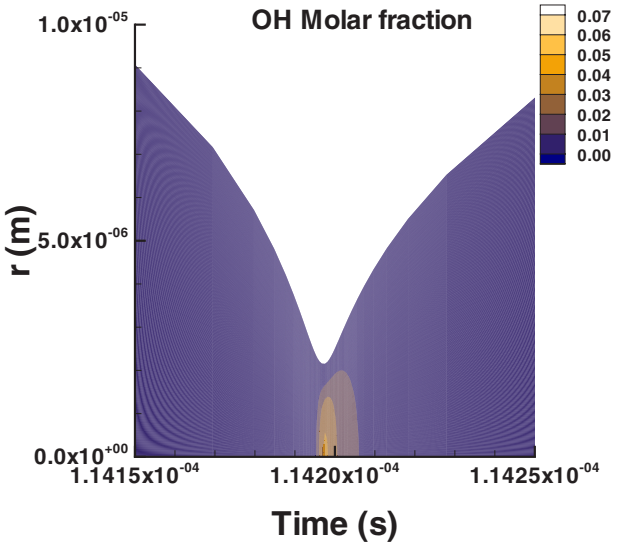

FIG. 19. (Color online) Main peak of the third series of rebounds. OH molar fraction profile during the bubble collapse.

bubble, the full reacting Navier-Stokes equations have been solved, whereas in the liquid, the complete energy equation together with a Rayeigh-Plesset equation have been used.

The dynamics have been coupled to thermochemical and transport phenomena across the bubble interface. To enhance the accuracy of the interface dynamics, an arbitrary Lagrangian-Eulerian formulation is implemented. Thus, temperatures at the interface are predicted without relying on empirical heat transfer coefficients. Accurate simulations of mass transfer across the bubble interface including water evaporation and condensation, vital in order to predict the OH formation, are also possible.

The model has been applied to an inert Ar bubble, an Ar-H_2O bubble with dissociation reactions, and a reacting H_2-O_2-Ar bubble. Space-time distributions of all the fluid variables have been predicted along several series of rebounds during both expansion and implosion phases.

Although the hypothesis of pressure uniformity has been confirmed for an inert bubble, it has been shown that mass transfer can slightly increase the gas interfacial pressure, producing larger bubble radii and stronger bubble implosions. Moreover, it has been found that reaction processes can induce important pressure gradients inside the bubble during the implosion. These pressure differences will depend on the reactions and the concentrations.

The results show that the radial dependence cannot be ignored if an accurate description of the chemistry inside the bubble is sought; the variation of the properties inside the bubble has an important impact on the progress of the chemical reactions, the consumption of reactants, and the production of radicals. For the reacting bubble, the radial distribution of the reaction rate modifies all variable profiles.

Different reaction zones have been encountered inside the bubble, where endothermic and exothermic processes can simultaneously take place. The radicals formed at the center in an endothermic process diffuse toward the interface, where they are recombined exothermically. When combustion occurs, it starts at the center, where the conditions are more extreme; the limiting reactant is exhausted at the center earlier than at the interface. It is then possible to find endothermic zones at the bubble center if the reactants have been exhausted before flame front propagation.

The evaporation and condensation have also been seen to determine the temperature at the interface, and the water content inside the bubble. Furthermore, they are responsible for decreasing the interface temperature (and increasing the liquid temperature) to values in agreement with experimental observations. Some results on stages of evaporation and condensation along a rebound have been presented. This work predicts that during the rebounds complex condensation and evaporation patterns can take place. This is essential in order

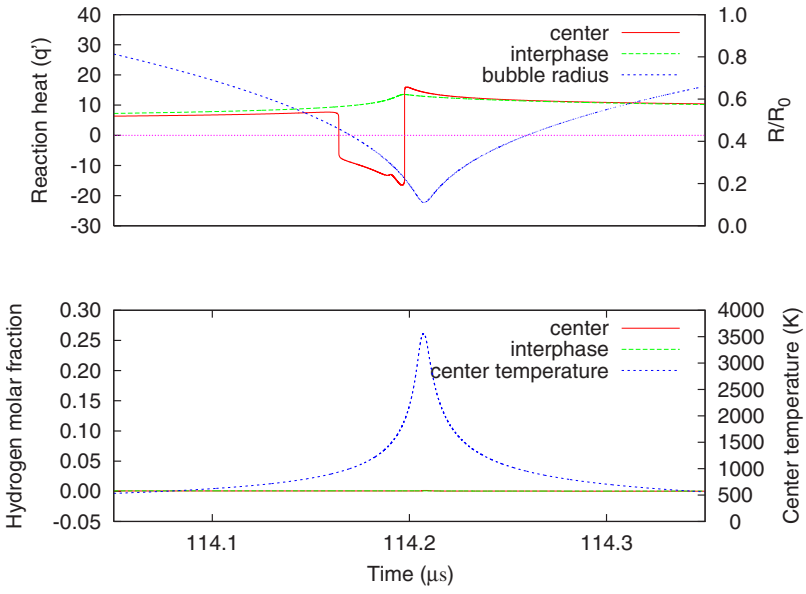

FIG. 20. (Color online) Evolution of the concentrations and reaction heat in the main peak of the third series.

to feed water into the bubble, as well as to predict the OH formation. For the cases analyzed, with water as the liquid, it has been found that, approximately, bubble compression is coupled with condensation and bubble expansion with evaporation.

ACKNOWLEDGMENTS

This work has been partially supported by Ministerio de Ciencia y Tecnologia, under Grant No. CTM2004-06184-C02-02.

[1] L. Rayleigh, Philos. Mag. **34**, 94 (1917).
[2] T. Lesko, Ph.D. thesis, California Institute of Technology, Pasadena, California, 2004.
[3] I. Hua, R. Höchemer, and M. Hoffmann, J. Phys. Chem. **99**, 2335 (1995).
[4] A. Colussi and M. Hoffmann, J. Phys. Chem. A **103**, 2696 (1999).
[5] A. Prosperetti, J. Acoust. Soc. Am. **56**, 878 (1974).
[6] A. Prosperetti, Ultrasonics **22**, 69 (1984).
[7] A. Prosperetti, L. Crum, and K. Commander, J. Acoust. Soc. Am. **83**, 502 (1988).
[8] V. Kamath, A. Prosperetti, and F. Egolfopoulos, J. Acoust. Soc. Am. **94**, 248 (1993).
[9] S. Sochard, A.-M. Wilhelm, and H. Delmas, Ultrason. Sonochem. **4**, 77 (1997).
[10] I. Akhatov, O. Landau, A. Topolnikov, R. Mettin, N. Vakhitova, and W. Lauterborn, Phys. Fluids **13**, 2805 (2001).
[11] C. Gong, Ph.D., MIT 1999.
[12] A. G. G. Nail, A. Gumerov, and Chao-Tsung Hsiao, California Institute of Technology and, Dynaflow, Inc., Technical Report No. 98001, 2001 (unpublished); see also http://gltrs.grc.nasa.gov/GLTRS.
[13] H. Lin, B. D. Storey, and A. J. Szeri, J. Fluid Mech. **452**, 145 (2002).
[14] N. Xu, R. Apfel, A. Khong, X. Hu, and L. Wang, Phys. Rev. E **68**, 016309 (2003).
[15] Y. An and C. Ying, Phys. Rev. E **71**, 036308 (2005).
[16] B. D. Storey and A. Szeri, Proc. R. Soc. London, Ser. A **456**, 1685 (2000).
[17] K. Yasui, T. Tuziuti, M. Sivakumar, and Y. Iida, J. Chem. Phys. **122**, 1 (2005).
[18] B. D. Storey and A. Szeri, J. Fluid Mech. **396**, 203 (1999).
[19] B. D. Storey and A. Szeri, Phys. Rev. Lett. **88**, 074301 (2002).
[20] A. Colussi and M. Hoffmann, J. Phys. Chem. A **103**, 11336 (1999).
[21] T. Hughes, W. Liu, and T. Zimmerman, Comput. Methods Appl. Mech. Eng. **29**, 329 (1981).
[22] J. Donea and A. Huerta, *Finite Element Methods for Flow Problems* (Wiley, Chichester, U.K., 2003).
[23] M. Plesset, J. Appl. Mech. **16**, 228 (1949).
[24] J. Keller and M. Miksis, J. Acoust. Soc. Am. **68**, 628 (1980).
[25] K. Yasui, Phys. Rev. E **56**, 6750 (1997).
[26] S. Sochard, A.-M. Wilhelm, and H. Delmas, Chem. Eng. Sci. **53**, 239 (1998).
[27] M. Knudsen, Ann. Phys. **47**, 697 (1915).
[28] H. Hertz, Ann. Phys. **17**, 177 (1982).
[29] R. Reidi, T. Sherwood, and J. Prausnitz, *The Properties of Gases and Liquids* (Mc-Graw Hill, New York, 1977).
[30] G. Narsimhan, Br. Chem. Eng. **10**, 253 (1965).
[31] W. Press, S. Teulkolsky, W. Vetterling, and B. Flannery, *Numerical Recipes in Fortran 77* (Cambridge University Press, Cambridge, U.K., 1992).
[32] W. C. Moss, D. A. Young, J. A. Harte, J. L. Levatin, B. F. Rozsnyai, G. B. Zimmerman, and I. H. Zimmerman, Phys. Rev. E **59**, 2986 (1999).
[33] A. Colussi, L. Weavers, and M. Hoffmann, J. Phys. Chem. A **102**, 6927 (1998).
[34] M. Allen, R. Yetter, and F. Dryer, Int. J. Chem. Kinet. **27**, 883 (1995).
[35] R. Akbar, M. Kaneshige, E. Schultz, and J. Sheperd, California Institute of Technology, Explosion Dynamics Laboratory Report No. FM97-3, 2000 (unpublished).